ACS Catalysis

Research Article

pubs.acs.org/acscatalysis

MnO_x-Promoted PdAg Alloy Nanoparticles for the Additive-Free Dehydrogenation of Formic Acid at Room Temperature

Ahmet Bulut,[†] Mehmet Yurderi,[†] Yasar Karatas,[†] Zafer Say,[‡] Hilal Kivrak,[§] Murat Kaya,[∥] Mehmet Gulcan,[†] Emrah Ozensoy,[‡] and Mehmet Zahmakiran*[,†]

[†]Nanomaterials and Catalysis (NanoMatCat) Research Laboratory, Department of Chemistry, Yüzüncü Yıl University, 65080, Van, Turkey

[‡]Department of Chemistry, Bilkent University, 06800, Ankara, Turkey

[§]Department of Chemical Engineering, Yüzüncü Yıl University, 65080, Van, Turkey

[∥]Department of Chemical Engineering and Applied Chemistry, Atılım University, 06836, Ankara, Turkey

Supporting Information

ABSTRACT: Formic acid (HCOOH) has a great potential as a safe and a convenient hydrogen carrier for fuel cell applications. However, efficient and CO-free hydrogen production through the decomposition of formic acid at low temperatures (<363 K) in the absence of additives constitutes a major challenge. Herein, we present a new heterogeneous catalyst system composed of bimetallic PdAg alloy and MnO_x nanoparticles supported on amine-grafted silica facilitating the liberation of hydrogen at room temperature through the dehydrogenation of formic acid in the absence of any additives with remarkable activity (330 mol H_2·mol catalyst^{-1}·h^{-1}) and selectivity (>99%) at complete conversion (>99%). Moreover this new catalytic system enables facile catalyst recovery and very high stability against agglomeration, leaching, and CO poisoning. Through a comprehensive set of structural and functional characterization experiments, mechanistic origins of the unusually high catalytic activity, selectivity, and stability of this unique catalytic system are elucidated. Current heterogeneous catalytic architecture presents itself as an excellent contender for clean hydrogen production via room-temperature additive-free dehydrogenation of formic acid for on-board hydrogen fuel cell applications.

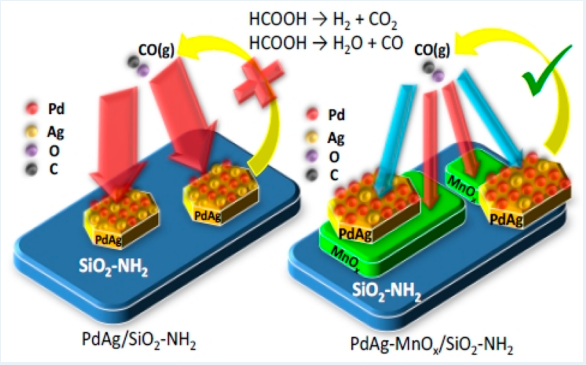

KEYWORDS: *formic acid, palladium, silver, alloy, manganese, dehydrogenation*

INTRODUCTION

Hydrogen (H_2) is considered to be a promising energy carrier due to its high energy density (142 MJ/kg), which is almost 3 times higher than that of natural gas (55 MJ/kg).[1,2] Furthermore, hydrogen is also an environmentally friendly energy vector as the utilization of hydrogen in proton exchange membrane fuel cells (PEMFC) generates only water as the chemical product.[3] However, controlled storage and release of hydrogen are still among the critical technological barriers faced by the hydrogen economy.[1−3] In this context, formic acid (HCOOH, FA), which is one of the major stable and nontoxic products formed in biomass processing, has recently attracted significant attention as a potential hydrogen carrier for fuel cells designed toward portable use.[4,5] In the presence of metal catalysts, FA can be decomposed catalytically via dehydrogenation (**1**) and/or dehydration (**2**) pathways.

$$HCOOH \rightarrow H_2 + CO_2 \quad \Delta G^{\circ}_{298K} = -35.0\ kJ/mol \tag{1}$$

$$HCOOH \rightarrow H_2O + CO \quad \Delta G^{\circ}_{298K} = -14.9\ kJ/mol \tag{2}$$

The selective dehydrogenation of FA is vital for the production of ultrapure H_2, because toxic carbon monoxide (CO) produced by the dehydration pathway significantly reduces the activity of the precious metal catalysts in PEMFC.[6] Recently, serious efforts have been focused on the development of homogeneous catalysts for the selective dehydrogenation of FA.[7−11] Even though notable catalytic performances have been reported in some of these studies,[12−14] the significant challenges associated with the catalyst isolation and recovery processes substantially hinder the practical use of such systems in on-board applications. Along these lines, numerous recent studies focused on the development of practical heterogeneous catalysts[15−26] exhibiting significant activity under mild conditions with high selectivity and facile catalyst recovery capabilities. In spite of these numerous former efforts, the majority of the heterogeneous catalysts reported in the literature for FA dehydrogenation require elevated temper-

Received: May 30, 2015
Revised: September 9, 2015
Published: September 9, 2015

ACS Publications © 2015 American Chemical Society

DOI: 10.1021/acscatal.5b01121
ACS Catal. 2015, 5, 6099−6110

atures and the utilization of extra additives (e.g., HCOONa, NR_3, $LiBF_4$ etc.),[27−29] while revealing low turnover frequency (TOF) values and limited reusability.[16−18,20−22] Until now, only a few Pd-based heterogeneous catalysts have been found to provide notable activities in the additive-free FA dehydrogenation at low temperatures.[19,23−25] In this regard, the development of highly active, selective, and reusable solid catalysts operating at low temperatures in the additive-free dehydrogenation of FA bears an enormous technological importance. Of particular importance, our recent study[24] has showed that Pd and MnO_x nanoparticles existing as a physical mixture on the surface of amine-grafted silica catalyze the additive-free FA dehydrogenation with 82% conversion and at room temperature. Moreover, the kinetic control experiments coupled with spectroscopic and electrochemical studies have led to the following important insights; (*i*) MnO_x nanoparticles (NPs) act as CO-sponges around the catalytically active Pd NPs and improve their operational performance in the FA dehydrogenation, (*ii*) the surface-grafted amine groups on SiO_2 support enhance the activity of Pd NPs by influencing the FA adsorption/storage process as well as the nucleation and growth of the Pd and MnO_x nanoparticles. These important findings have fostered us to use MnO_x and amine-grafted SiO_2 support for the development of new Pd-based heterogeneous catalytic systems for the additive-free dehydrogenation of FA.

Along these lines, in this study we present a facile synthetic route for obtaining PdAg alloy and MnO_x NPs supported on aminopropyl-functionalized silica, which will hereafter be referred to as PdAg-MnO_x/N-SiO_2. Furthermore, we show the remarkable catalytic performance of this novel material architecture in the additive-free decomposition of FA at room temperature via pathway (**1**) with high reusability performance. PdAg-MnO_x/N-SiO_2 catalyst was prepared with high reproducibility through a simple impregnation route followed by subsequent sodium borohydride ($NaBH_4$) reduction in water at room temperature. The structural characterization of PdAg-MnO_x/N-SiO_2 was performed by using a multitude of analytical techniques including inductively coupled plasma-optical emission spectroscopy (ICP-OES), powder X-ray diffraction (XRD), in situ Fourier transform infrared spectroscopy (in situ FTIR), X-ray photoelectron spectroscopy (XPS), diffuse reflectance UV−vis (DR-UV−vis) spectroscopy, transmission electron microscopy (TEM), high-resolution transmission electron microscopy (HRTEM), scanning transmission electron microscopy-energy dispersive X-ray spectroscopy (STEM-EDX), high-angle annular dark field-scanning transmission electron microscopy (HAADF-STEM), linear sweep voltammetry (LSV), CO-stripping voltammetry and N_2-adsorption−desorption techniques. Comprehensive structural characterization efforts presented in the current contribution indicate the presence of separate PdAg alloy and MnO_x NPs, which nucleate on the surface of the aminopropyl-functionalized silica support surface and interact efficiently in a synergistic manner. The resulting PdAg-MnO_x/N-SiO_2 material can catalyze dehydrogenation of FA in the absence of additives with the high activity (turnover frequency (TOF) = 330 h^{-1}) even at room temperature. Moreover, the exceptional durability of PdAg-MnO_x/N-SiO_2 against agglomeration, leaching, and CO poisoning renders this catalytic architecture an excellent contender as a reusable heterogeneous catalyst in the hydrogen production from formic acid for on-board fuel cell applications.

EXPERIMENTAL SECTION

Materials. Palladium(II) nitrate dihydrate ($Pd(NO_3)_2.2H_2O$) (~40% Pd basis), manganese(II) nitrate tetrahydrate ($Mn(NO_3)_2{\cdot}4H_2O$), silver(I) nitrate ($AgNO_3$), aminopropyltriethoxysilane ($H_2N(CH_2)_3Si(OC_2H_5)_3$, APTS), sodium borohydride ($NaBH_4$), ninhydrin ($C_9H_6O_4$), toluene (C_7H_8), and sodium hydroxide (NaOH) were purchased from Sigma-Aldrich. Formic acid (CH_2O_2, > 96%) and silica gel (230−400 mesh) were purchased from Merck. Toluene was distilled over sodium and stored in a Labsconco nitrogen-atmosphere drybox (O_2< 1 ppm). Deionized water was distilled by water purification system (Milli-Q Water Purification System). All glassware and Teflon-coated magnetic stirring bars were washed with acetone and copiously rinsed with distilled water before drying in an oven at 423 K.

Characterization. Pd, Ag, and Mn contents of the samples were determined by ICP-OES (Leeman, Direct Reading Echelle) after each sample was completely dissolved in a mixture of HNO_3/HCl (1/3 v/v). Powder X-ray diffraction (XRD) patterns were recorded with a MAC Science MXP 3TZ diffractometer using Cu Kα radiation (wavelength 1.54 Å, 40 kV, 55 mA). TEM, HRTEM, STEM, and HAADF-STEM samples were prepared by dropwise addition of the dilute catalyst suspension on a copper-coated carbon TEM grid followed by the evaporation of the solvent. The conventional TEM measurements were carried out on a JEOL JEM-200CX transmission electron microscope operating at 120 kV. HRTEM, STEM, and HAADF-STEM analysis were performed using a JEOL JEM-2010F transmission electron microscope operating at 200 kV. Oxford EDX system and the Inca software were exploited to acquire and process STEM-EDX data. The XPS measurements were employed via a Physical Electronics 5800 XP spectrometer equipped with a hemispherical analyzer and a monochromatic Al Kα X-ray source (1486.6 eV, 15 kV, 350 W, with pass energy of 23.5 eV). Gas-phase decomposition products of formic acid were analyzed by gas chromatography using FID-2014 and TCD-2014GC analyzers (Shimadzu). UV−vis electronic absorption spectra were recorded on a Shimadzu UV-2600 spectrophotometer.

Catalyst Preparation. The functionalization of the silica was carried out by adding a desired amount of APTS to 30 mL of dry toluene containing 500 mg of silica. The resulting slurry was stirred for 12 h. The white solid was filtered and washed repeatedly with toluene. The white amine-functionalized silica (SiO_2−NH_2) was dried in a vacuum oven (373 K and 10^{-1} Torr) and used for further application. The presence of $-NH_2$ functionalities on the SiO_2 support surface was quantified by the colorimetric ninhydrin method.[30] PdAg-MnO_x/N-SiO_2 catalyst was obtained by the conventional impregnation and subsequent reduction steps.[31] Typically, 5.0 mL aqueous solution containing $Pd(NO_3){\cdot}2H_2O$ (6.24 mg, 23.4 μmol Pd), $AgNO_3$ (0.80 mg, 4.7 μmol Ag), $Mn(NO_3)_2{\cdot}4H_2O$ (4.7 mg, 18.7 μmol Mn) and SiO_2−NH_2 (100 mg, 100 μmol NH_2) is mixed for 3 h. Then, the fresh 1.0 mL aqueous solution of $NaBH_4$ (28 mg, 0.7 mmol) was added to this mixture and the resulting solution was stirred for half an hour under ambient conditions. After centrifugation (6000 rpm, 5 min), copious washing with water (3 × 20 mL), filtration, and drying in oven at 373 K, PdAg-MnO_x/N-SiO_2 catalyst was obtained as a dark gray powder.

Activity Measurements. The catalytic activity of Pd-MnO_x/SiO_2−NH_2 in the additive-free FA dehydrogenation was

DOI: 10.1021/acscatal.5b01121
ACS Catal. 2015, 5, 6099−6110

determined by volumetric measurement of the rate of hydrogen evolution. The volume of released gas during the reaction was monitored using a gas buret through water displacement as described elsewhere.[15−25] Before starting the catalytic activity tests, a jacketed one-necked reaction flask (50.0 mL) containing a Teflon-coated stirring bar was placed on a magnetic stirrer (Heidolph MR-3004) whose temperature was adjusted by circulating water through its jacket from a constant temperature bath (Lab Companion RW-0525). In a typical catalytic activity test, PdAg-MnO_x/N-SiO_2 catalyst was weighed and transferred into the reaction flask, and then 9.0 mL H_2O was added into the reaction flask followed by rigorous stirring for 15 min to achieve thermal equilibrium. Next, 0.5 mL of aqueous FA solution (0.1 mL FA + 0.4 mL H_2O) was added into the reaction flask via its septum using a 1.0 mL gastight syringe, and the catalytic reaction was started (t = 0 min) by stirring the mixture at 600 rpm.

Catalytic Selectivity. The selectivity of PdAg-MnO_x/N-SiO_2 catalyst in the decomposition of FA was investigated by GC analysis and NaOH-trap experiments. The gas generated over PdAg-MnO_x/SiO_2−NH_2 catalyzed dehydrogenation of aqueous FA solution (10.0 mL of 0.3 M) was collected in a GC analyzing balloon, which was then analyzed in GC by using pure CO, H_2 and CO_2 as reference gases. NaOH-trap experiments were performed to determine the molar ratio of CO_2 to H_2 in the product mixture generated during the PdAg-MnO_x/SiO_2−NH_2 catalyzed decomposition of aqueous FA solution (10 mL of 0.3 M).[15−25] In these experiments, the trap (10.0 M NaOH solution) was placed between the jacketed reactor and gas buret. The generated gas during the reaction was passed through the NaOH trap where CO_2 was captured (**3**). Next, the volume of the gas generated from the dehydrogenation of FA was monitored and compared to those without the trap experiment. We observed that the volume of the generated gas decreased by a factor of 2 in the presence of the NaOH trap. This result is indicative of the complete adsorption of CO_2 in NaOH solution (**3**) and the presence of equivalent molar amounts of CO_2 and H_2 (1.0:1.0) in the product mixture of the PdAg-MnO_x/SiO_2−NH_2 catalyzed additive-free FA dehydrogenation.

$$2NaOH + CO_2 \rightarrow Na_2CO_3 + H_2O \quad (3)$$

Catalytic Stability. The recyclability of PdAg-MnO_x/N-SiO_2 in the additive-free dehydrogenation of FA was determined by a series of experiments started with a 10.0 mL aqueous FA solution (0.1 mL of FA + 9.9 mL of H_2O) at 298 K. Immediately after the achievement of complete conversion, another equivalent amount of FA was added to the reaction mixture, leading to further hydrogen evolution. The same procedure was repeated up to the fifth subsequent catalytic recycle. In the reusability experiments, the catalyst was isolated from the reaction solution by centrifugation after the first catalytic run and washed with excess water and dried at 373 K. The dried catalyst was weighed and reused in the catalytic dehydrogenation of a 10.0 mL aqueous FA solution (0.1 mL FA + 9.9 mL H_2O) at 298 K. This identical catalyst was isolated and reused up to 5 consecutive catalytic cycles.

Cyclic Voltammetry (CV) Measurements. CV measurements were carried out in a conventional three-electrode cell with a Pt wire as the counter electrode and Ag/AgCl as the reference electrode with a CHI 660E potentiostat. The working electrode was a glassy carbon disk having a diameter of 3.0 mm held in a Teflon cylindrical housing. Before the CV measurements, the surface of the glassy carbon electrode was polished with alumina to prepare the surface of the electrode for the catalyst deposition process. For the electrode preparation, typically 7−9 mg of catalyst was dispersed in a 1.0 mL 5% Nafion medium (Aldrich) to obtain a catalyst suspension. Then, 6.0 μL of this suspension was drop-cast on the surface of the glassy carbon electrode. Then, the electrode was dried at room temperature to remove the solvent. CV's were recorded between −0.23 and 1.0 V with a scan rate of 10 mV s^{-1} in the presence of 0.5 M H_2SO_4 and 1.0 M HCOOH. Prior to the CV experiments, the electrolyte was saturated with N_2, and the electrode surface was activated via 0.5 M H_2SO_4.

Linear Sweep Voltammetry (LSV) Measurements. Linear sweep voltammetry (LSV) technique was employed to investigate the CO adsorption on the PdAg/SiO_2−NH_2 and PdAg-MnO_x/SiO_2−NH_2 catalyst surface, which can poison the surface during the decomposition of formic acid.[32,33] Before the LSV measurements, catalysts were exposed to a pretreatment process, where the catalyst surfaces were maintained at a constant potential of 0.0 V for 180 s. After the pretreatment, LSV measurements were carried out to determine the activity of the pretreated surfaces in the electrocatalytic oxidation of FA. These measurements were conducted within the bias range of −0.2 to 0.9 V in a solution containing 0.5 M H_2SO_4 and 1.0 M HCOOH using a 10 mV s^{-1} scan rate.

CO-Stripping Voltammetry Measurements. Five milligrams of catalyst sample was dispersed in 1.0 mL of 5% Nafion solution (Aldrich) to obtain a catalyst suspension. Next, 5.0 μL of this suspension was drop-cast on the surface of the glassy carbon electrode. All electrolyte solutions were deaerated with high-purity nitrogen for 30 min prior to the measurements. For CO stripping voltammetry, 0.5 M H_2SO_4 solution was first bubbled with pure nitrogen for 30 min in order to remove the dissolved oxygen. CO was then purged into the solution for 20 min to allow saturation of the electrocatalyst surface with adsorbed CO, while maintaining a constant potential of 0 0.0 V. Excess CO was then purged with nitrogen for 30 min.

In Situ FTIR Spectroscopic Analyses. Detailed description of the instrumentation used in the currently presented in situ FTIR experiments can be found elsewhere.[34] Briefly, in situ FTIR spectroscopic measurements were performed in transmission mode using a Bruker Tensor 27 FTIR spectrometer, which was modified to house a batch-type custom-made in situ spectroscopic reactor. All catalysts were initially cleaned by annealing under vacuum (<1 × 10^{-3} Torr) at 400 K for 2 h. This process is needed to thermally remove the adsorbed water on the material surfaces and obtain materials that are relatively more transparent to the IR beam. CO adsorption (poisoning) experiments were performed by introducing 20.0 Torr of CO (>99.995% purity, Air Products) for 10 min at 323 K followed by evacuation at ∼10^{-3} Torr. FA adsorption was performed on CO preadsorbed (i.e., poisoned) catalyst surfaces where the FTIR spectra for the CO-poisoned surfaces were used as the corresponding background spectra. In this set of experiments, after 20.0 Torr of CO adsorption at 323 K for 10 min, 5.0 Torr of FA was dosed on the poisoned catalysts for 5 min. Next, the reactor was evacuated (P < 10^{-2} Torr), and FTIR spectra were acquired. All FTIR spectra in this study were collected at 323 K.

RESULTS AND DISCUSSION

Catalyst Preparation and Characterization. PdAg-MnO_x/N-SiO_2 catalyst can be prepared simply and reproducibly by following the procedure comprising the conventional

DOI: 10.1021/acscatal.5b01121
ACS Catal. 2015, 5, 6099−6110

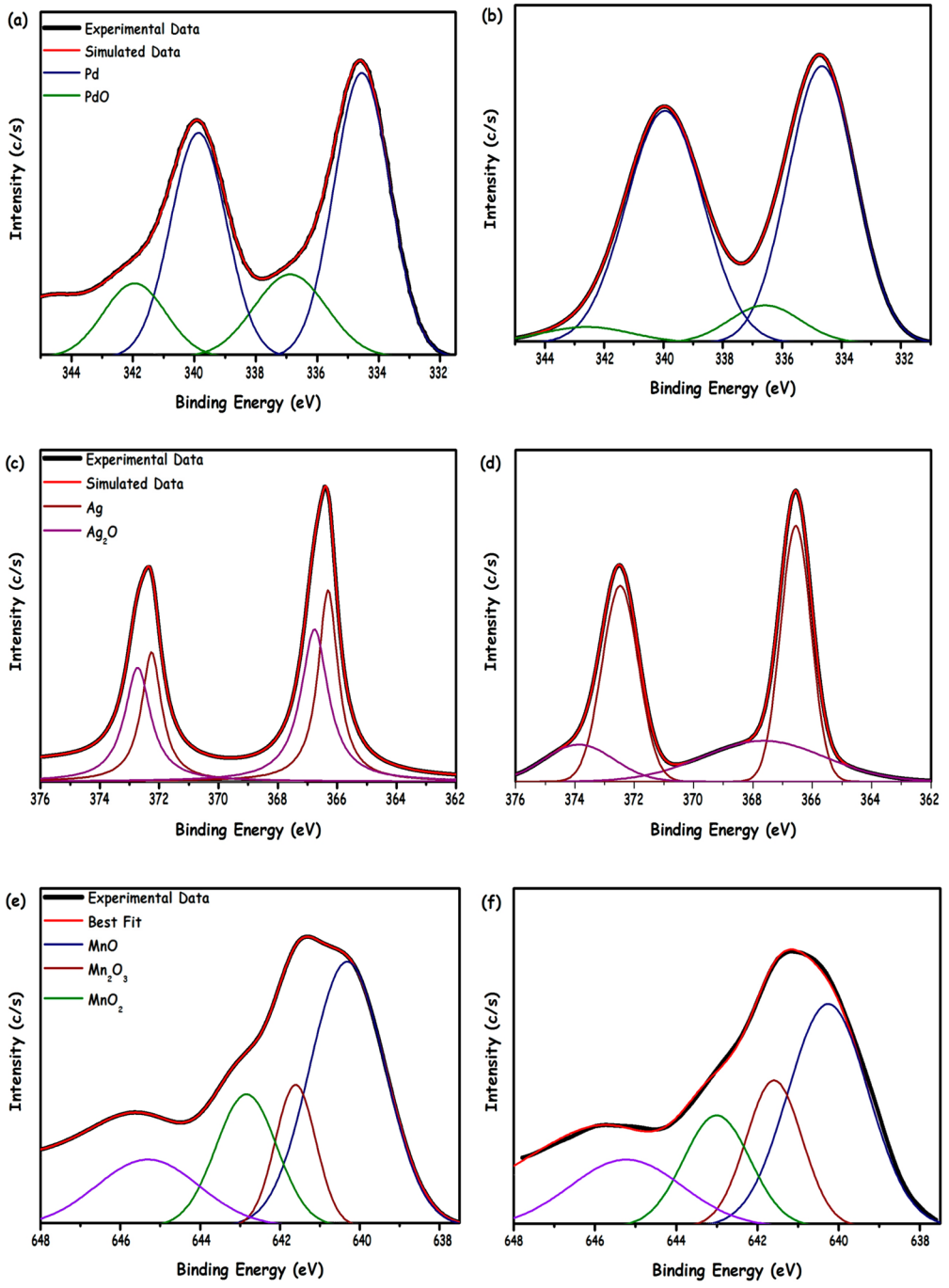

Figure 1. Pd 3d XP spectra (a) before, (b) after (5 min) Ar^+(g) sputtering; Ag 3d XPS spectra (c) before, (d) after (5 min) Ar^+(g) sputtering; Mn 2p XP spectra (e) before, (f) after (5 min) Ar^+(g) sputtering for PdAg-MnO_x/N-SiO_2 catalyst.

impregnation[31] of Pd^{2+}, Ag^+, and Mn^{2+} onto amine-functionalized silica and their borohydride reduction at room temperature. After centrifugation and copious washing with water, PdAg-MnO_x/N-SiO_2 catalyst was isolated as a gray powder and characterized by multipronged techniques. The elemental composition of the as-prepared PdAg-MnO_x/SiO_2–NH_2 catalyst was found to be $Pd_{0.44}Ag_{0.19}Mn_{0.37}$ (i.e., 1.27 wt % Pd, 0.57 wt % Ag, and 0.54 wt % Mn; corresponding to relative molar amounts of 11.9 μmol Pd, 5.3 μmol Ag, 9.8 μmol Mn, and 0.98 mmol NH_2/g SiO_2) by ICP-OES analyses and ninhydrin method.[30] The survey XPS spectrum of PdAg-MnO_x/SiO_2–NH_2 catalyst (Figure S1) shows the existence of Pd, Ag, and Mn with the elements of support material (Si, O, C and N). Pd 3d, Ag 3d and Mn 2p XPS spectra of the PdAg-MnO_x/SiO_2–NH_2 catalyst together with their deconvoluted chemical states are given in Figure 1a,c,e. These results reveal the presence of metallic (i.e., Pd^0 with Pd $3d_{5/2}$ at 334.5 eV and Pd $3d_{3/2}$ at 339.8 eV), as well as oxidic (i.e., Pd^{2+} with Pd $3d_{5/2}$ at 336.9 eV and Pd $3d_{3/2}$ at 341.9 eV) Pd states.[35] Ag was also found to be in both metallic (i.e., Ag^0 with Ag $3d_{5/2}$ 366.8 eV and Ag $3d_{3/2}$ 372.8 eV) and oxidic (i.e., Ag^+ with Ag $3d_{5/2}$ 366.5 eV; Ag $3d_{3/2}$ 372.9 eV) states.[36] On the other hand, Mn was found to exist in the form of Mn^{2+} (Mn $2p_{3/2}$ at 640.3 eV), Mn^{3+} (Mn $2p_{3/2}$ at 641.6 eV) and Mn^{4+} (Mn $2p_{3/2}$ at 642.8 eV)[37,38] exhibiting an additional high-binding energy shakeup peak feature at 645.5 eV.[38] XPS spectra presented in Figure

DOI: 10.1021/acscatal.5b01121
ACS Catal. 2015, 5, 6099–6110

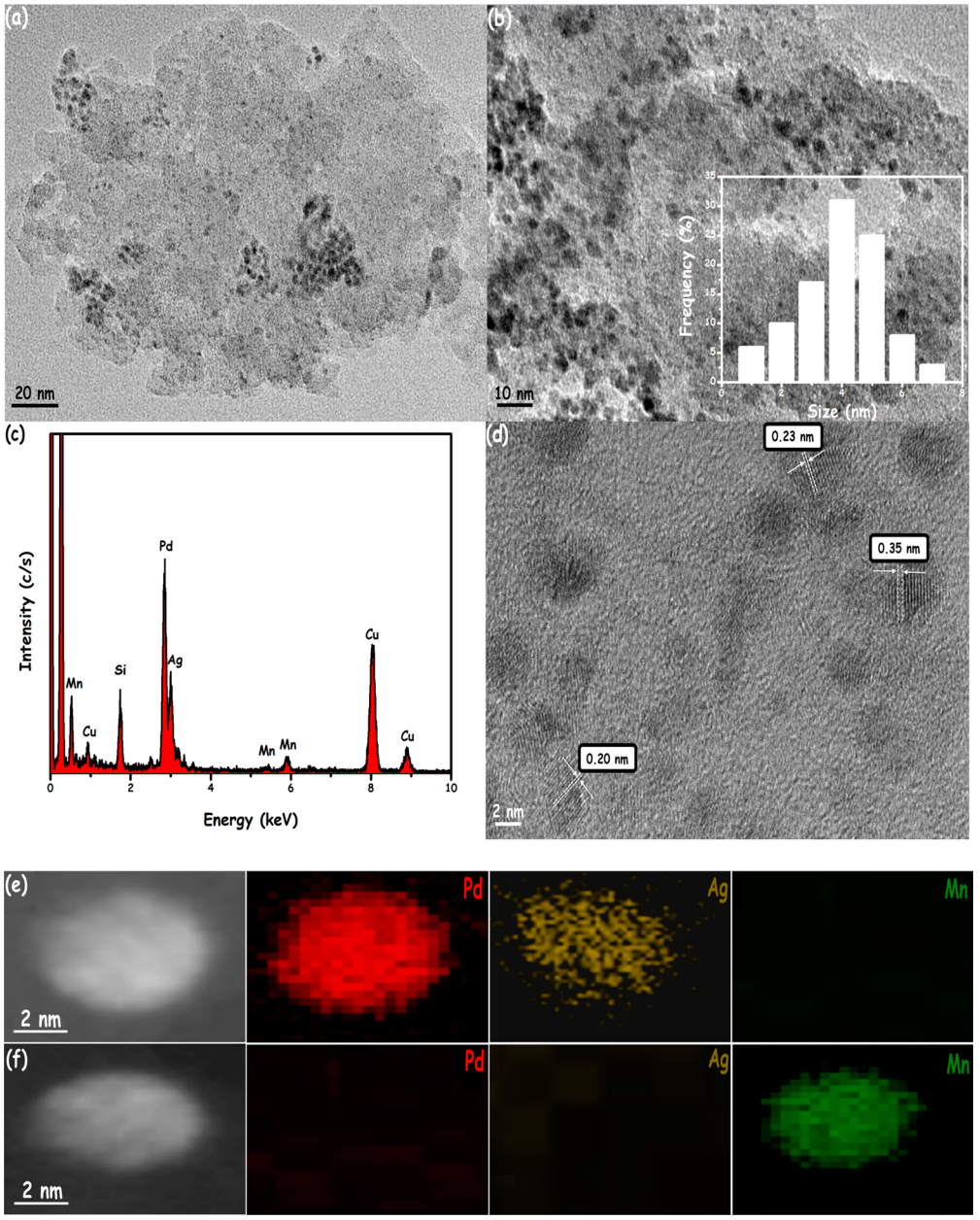

Figure 2. (a, b) TEM images and particle size distribution (inset in panel b), (c) TEM-EDX spectrum, (d) HRTEM image of the PdAg-MnOx/N-SiO_2 catalyst; (e) and (f) HAADF-STEM images, HAADF-STEM elemental mapping for Pd, Ag, and Mn of the PdAg-MnO_x/N-SiO_2 catalyst.

1b,d suggest that after Ar^+(g) sputtering for 5 min, XPS features associated with Pd^{2+} and Ag^+ could be removed where Pd^0 and Ag^0 exist as the predominant features. However, oxidic forms of Mn continue to exist even after Ar^+(g) sputtering (Figure 1f) without any major alteration. Existence of oxidic states of Mn is not unexpected as the high oxophilicity of Mn makes Mn^0 NPs highly reactive upon exposure to air leading to the generation of various forms of MnO_x states with high stability.[39,40]

TEM, HRTEM, STEM-EDX, and HAADF-STEM-mapping investigations were performed to examine the size, morphology, and the composition of the PdAg-MnO_x/N-SiO_2 catalyst. TEM images of PdAg-MnO_x/N-SiO_2 given in Figure 2a,b reveal the presence of PdAg and MnO_x nanoparticles (for comparison, see the TEM image of metal-free see N-SiO_2 is given in Figure S2). The mean particle size for the images given in Figure 2a,b was found to be ca. 6.4 nm using the NIH image program,[41] which included the particle size analysis for >100 nontouching particles (Figure 2b, inset). STEM-EDX analysis of a large number of different domains on the PdAg-MnO_x/N-SiO_2 surface confirmed the presence of Pd, Ag, and Mn in the analyzed regions (Figure 2c). HRTEM image of PdAg-MnO_x/N-SiO_2 is given in Figure 2d displaying the highly crystalline nature of the NPs on the PdAg-MnO_x/N-SiO_2 surface. Three different crystalline fringe distances (0.20, 0.23, and 0.35 nm) were measured for three individual NPs. The fringe distances of 0.20 and 0.35 nm can be assigned to MnO_2[42] and Mn_2O_3[43] phases, respectively. On the other hand, the fringe distance of 0.23 nm, which is between the (111) lattice spacing of face-centered cubic (fcc) Ag (0.24 nm) and fcc Pd (0.22 nm), can be attributed to a PdAg alloy structure. In addition to that, the XRD pattern of the as-synthesized catalyst (Figure S3) exhibits a diffraction peak located between the characteristic Pd (111) and Ag (111) diffraction features. DR-UV−vis spectrum taken from solid powders of PdAg-MnO_x/N-SiO_2 (Figure S4) shows

DOI: 10.1021/acscatal.5b01121
ACS Catal. 2015, 5, 6099−6110

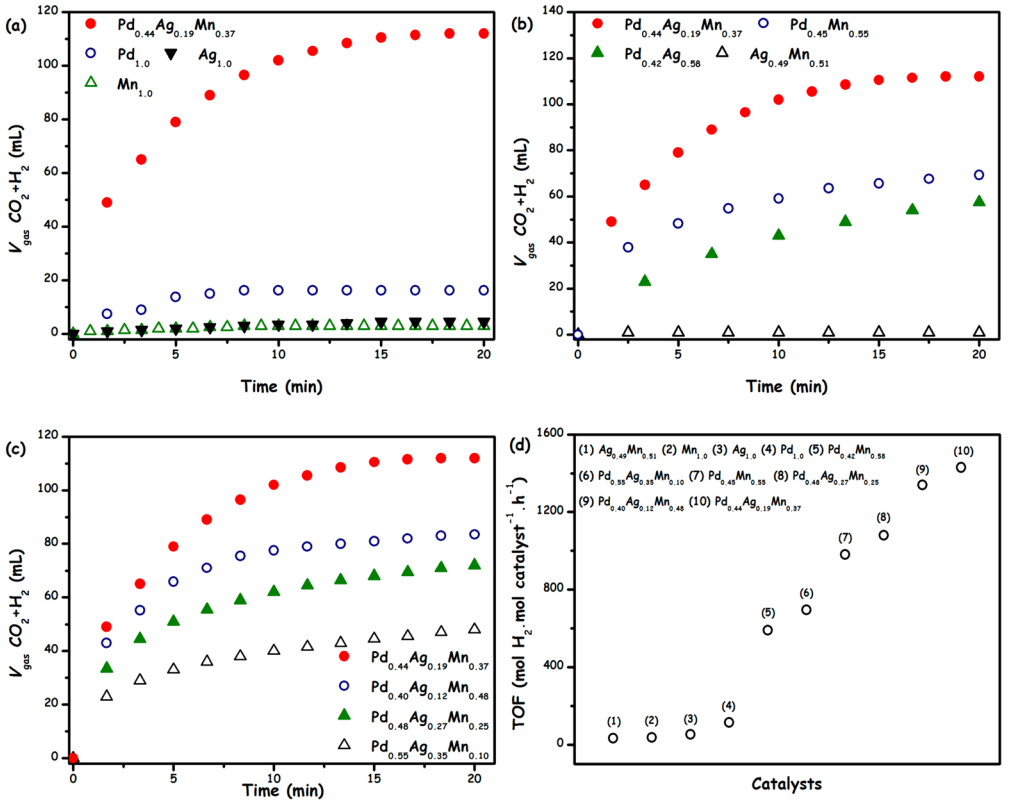

Figure 3. Volume of generated gas (CO_2 + H_2) (mL) versus time (min) graphs of (a) monometallic, (b) bimetallic, (c) trimetallic catalysts, (d) TOF values versus catalysts in different [Pd]:[Ag]:[Mn] ratios for the additive-free FA dehydrogenation (0.25 M in 10.0 mL H_2O) at 313 K.

a very weak surface plasmon resonance (SPR) feature, whereas Ag/SiO_2–NH_2 and Ag-MnO_x/N-SiO_2 samples reveal much stronger SPR bands at ca. 440 nm. It is worth mentioning that quenching of the SPR bands due to alloying was also observed for oleylamine-stabilized PdAg alloy NPs.[23]

The compositional analyses of the PdAg-MnO_x/N-SiO_2 catalyst were also performed by detailed HAADF-STEM measurements. Figure 2 also presents HAADF-STEM images (Figure 2e,f) as well as elemental mapping analysis of Pd, Ag, and Mn for two independent particles existing on the PdAg-MnO_x/N-SiO_2 catalyst surface. Although HAADF-STEM-elemental mapping suggests the existence of a PdAg alloy for the first particle in the absence of any Mn signal, the second particle reveals the exclusive presence of Mn lacking appreciable Pd or Ag signals. These results support the presence of individual PdAg alloy NPs that are separate from the MnO_x NPs on the N-SiO_2 support surface. On the other hand, as it is difficult to establish a true statistical analysis using microscopic probes, presence of a minor amount of overlapping domains of PdAg and MnO_x cannot be excluded.

Catalytic Performance Results. For a comprehensive elucidation of the catalytic activity of the PdAg-MnO_x/N-SiO_2 catalytic architecture toward additive-free dehydrogenation of FA, we followed a systematic approach, where the individual catalytic performance of each structural subcomponent (i.e., single-component samples such as $Pd_{1.0}$/N-SiO_2, $Ag_{1.0}$/N-SiO_2, $Mn_{1.0}$/N-SiO_2) was studied (Figure 3a–d) in addition to binary combinations of these subcomponents (i.e., $Pd_{0.45}$-$Mn_{0.55}$/N-SiO_2, $Pd_{0.42}Ag_{0.58}$/N-SiO_2, $Ag_{0.49}$-$Mn_{0.51}$/N-SiO_2) as well as their ternary counterparts (i.e., $Pd_{0.40}Ag_{0.12}$-$Mn_{0.48}$/N-SiO_2, $Pd_{0.44}Ag_{0.19}$-$Mn_{0.37}$/N-SiO_2, $Pd_{0.48}Ag_{0.27}$-$Mn_{0.25}$/N-SiO_2, $Pd_{0.55}Ag_{0.35}$-$Mn_{0.10}$/N-SiO_2). Evidently, $Pd_{0.44}Ag_{0.19}$-$Mn_{0.37}$/N-SiO_2 catalyst provides the best activity compared to all other investigated catalysts. Comparison of Figure 3a and Figure 3b strongly implies that Pd has a critical role in the FA decomposition, as the catalytic activity is completely lost in the absence of Pd (e.g., $Ag_{1.0}$/N-SiO_2, $Mn_{1.0}$/N-SiO_2, and $Ag_{0.49}$-$Mn_{0.51}$/N-SiO_2). On the other hand, the initially high activity of the single-component $Pd_{1.0}$/N-SiO_2 catalyst is not sustainable as the active sites can readily be deactivated due to the generation of a poisonous byproduct (i.e., CO), demonstrating the paramount challenges associated with the use of a single-component catalytic architecture in formic acid decomposition lacking additional promoters such as Ag and Mn.[4,5]

Although binary systems such as $Pd_{0.45}$-$Mn_{0.55}$/N-SiO_2 and $Pd_{0.42}Ag_{0.58}$/N-SiO_2 show better activities than $Pd_{1.0}$/N-SiO_2, their performances are still far inferior to the ternary $Pd_{0.44}Ag_{0.19}$-$Mn_{0.37}$/N-SiO_2 system (Figure 3). Morphological investigation by TEM (Figure S5) reveals that NPs of the single-component and binary systems have smaller particle sizes with respect to the ternary $Pd_{0.44}Ag_{0.19}$-$Mn_{0.37}$/N-SiO_2 system. The uniqueness of the $Pd_{0.44}Ag_{0.19}$-$Mn_{0.37}$/N-SiO_2 catalyst structure was further supported by two control experiments where physical mixture of (*i*) Pd/N-SiO_2, Ag/N-SiO_2, Mn/N-SiO_2 (with a Pd:Ag:Mn molar ratio of 0.45:0.21:0.34) and (*ii*) $Pd_{0.41}Ag_{0.59}$/N-SiO_2 and $Mn_{0.37}$/N-SiO_2 exhibited a lower activity than that of $Pd_{0.44}Ag_{0.19}$-$Mn_{0.37}$/N-SiO_2 catalyst in FA dehydrogenation in the absence of additives under identical conditions (Figure S6). These control experiments demonstrate a proximity requirement associated with the synergistic structural components of the $Pd_{0.44}Ag_{0.19}$-$Mn_{0.37}$/N-SiO_2 catalyst, which interact in an efficient manner during additive-free dehydrogenation of FA. The generated gas obtained via

DOI: 10.1021/acscatal.5b01121
ACS Catal. 2015, 5, 6099–6110

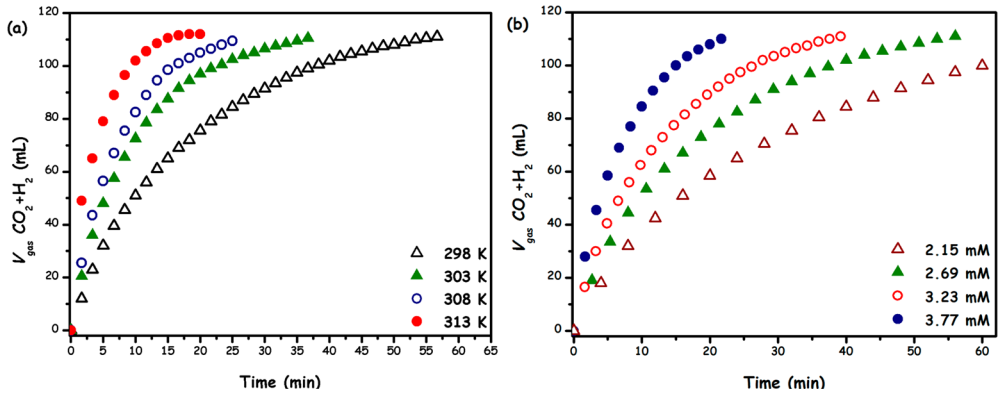

Figure 4. (a) Volume of the generated gas versus time plots for $Pd_{0.44}Ag_{0.19}$-$Mn_{0.37}$/N-SiO_2 (2.69 mM) catalyzed additive-free dehydrogenation of FA (0.25 M FA in 10.0 mL H_2O) at different temperatures, (b) analogous data for 0.25 M FA in 10.0 mL H_2O at 298 K corresponding to varying catalyst ($Pd_{0.44}Ag_{0.19}$-$Mn_{0.37}$/N-SiO_2) concentrations.

$Pd_{0.44}Ag_{0.19}$-$Mn_{0.37}$/N-SiO_2-catalyzed FA dehydrogenation was analyzed by gas chromatography (GC) in the presence or absence of the NaOH trap (Figure S7). These experiments revealed that the generated gas is a mixture of H_2 and CO_2 with a H_2:CO_2 molar ratio of 1.0:1.0 where CO was below the detection limit (i.e., < 10 ppm). In other words, these experiments point to the important fact that CO-free H_2 generation can be achieved in the absence of additives from an aqueous FA solution for fuel cell applications[6] at ambient conditions by utilizing a $Pd_{0.44}Ag_{0.19}$-$Mn_{0.37}$/N-SiO_2 catalyst.

Figure 4a shows the volume of generated gas (CO_2 + H_2) versus the reaction time for $Pd_{0.44}Ag_{0.19}$-$Mn_{0.37}$/N-SiO_2 catalyzed additive-free FA dehydrogenation at different temperatures. It is apparent that $Pd_{0.44}Ag_{0.19}$-$Mn_{0.37}$/N-SiO_2 catalyst provides *initial* TOF values of 330, 530, 700, 1430 mol H_2·mol catalyst^{-1}·h^{-1} at 298, 303, 308, and 313 K, respectively (see Supporting Information for details of the calculation of initial TOF values). The *initial* TOF value of 330 mol H_2·mol catalyst^{-1}·h^{-1} (corresponding to 750 mol H_2·mol Pd^{1-}·h^{-1} and 524 mol H_2·mol (Pd+Ag)$^{-1}$·h^{-1}, assuming that the active sites are only provided by Pd or PdAg NPs, respectively) measured at 298 K is one of the most remarkable TOF values reported for FA dehydrogenation at room temperature using a heterogeneous catalyst without utilizing any additives (Table 1).

More importantly, FA dehydrogenation can be completed in less than an hour with >99% conversion. The values of observed rate constants k_{obs} determined from the linear portions of the volume of generated gas (CO_2 + H_2) versus reaction time plots at four different temperatures are used to obtain Arrhenius and Eyring plots (Figure S8 and Figure S9) to calculate activation parameters. Using these plots, apparent activation energy (E_a), apparent activation enthalpy ($\Delta H_a^{\neq}$), and apparent activation entropy ($\Delta S_a^{\neq}$) values were calculated to be 72.4 kJ/mol, 69.1 kJ/mol, and 37.5 J/mol·K, respectively. The positive magnitude of the apparent activation entropy implies the presence of a dissociative mechanism in the transition state (vide infra).[44]

In addition to the effect of temperature, we also investigated the influence of the catalyst concentration on the rate of the additive-free dehydrogenation of FA by performing the catalytic reaction starting with different $Pd_{0.44}Ag_{0.19}$-$Mn_{0.37}$/N-SiO_2 concentrations at 298 K (Figure 4b). The reaction rates for each catalyst concentration were calculated from the linear portion of each plot given in Figure 4b. The logarithmic plot of the hydrogen generation rate versus catalyst concentration (Figure S10) gives a line with a slope of 1.18, which indicates that $Pd_{0.44}Ag_{0.19}$-$Mn_{0.37}$/N-SiO_2 catalyzed additive-free FA dehydrogenation, is close to first-order with respect to the catalyst concentration within the investigated concentration window.

Table 1. Comparison of the Catalytic Performance Data for the Currently Studied PdAg-MnO_x/N−SiO_2 Catalyst with the Prior Best Heterogeneous Catalyst Systems Reported for the Dehydrogenation of FA in the Absence of Any Additives at Low Temperatures

catalyst	temp (K)	conv. (%)	activity (h^{-1})[a]	ref
Ag@Pd	293	36	63	18
AgPd	293	10	72	18
Au@Pd	298	89	98	19
CoAuPd/C	298	91	37	20
CoAuPd/GO	298	51	45	21
CoAuPd/DNA	298	96	85	21
AuPd	298	28	41	22
AgPd	298	52	180	23
Pd-MnO_x	298	63	150	24
PdAu-MnO_x/MOF-graphene	298	94	382[b]	25
PdAuCr/N-SiO_2	298	99	730	26
PdAg-MnO_x/N-SiO_2	298	99	524[c]	this study
PdAg-MnO_x/N-SiO_2	298	99	330	this study

[a]TOF = mol H_2/mol total metal × h, and these TOF values are not corrected for the number of exposed surface atoms; that is, the values given are lower limits. [b]Based on Au and Pd atoms. [c]Based on Ag and Pd atoms.

The catalytic stability of the PdAg-MnO_x/N-SiO_2 catalyst in the additive-free dehydrogenation of FA was investigated by performing recycling and reusability experiments. When all of FA was converted to CO_2 and H_2 in a particular cycle, more FA was added into the solution, and the reaction was continued up to five consecutive catalytic cycles. It was found that PdAg-MnO_x/N-SiO_2 catalyst (i.e., $Pd_{0.44}Ag_{0.19}$-$Mn_{0.37}$/N-SiO_2) retains 86% of its initial activity and provides 98% of conversion without CO generation after the fifth consecutive cycle (Figure 5a). Ease of isolation and reusability characteristics of PdAg-MnO_x/N-SiO_2 were also tested in the FA dehydrogenation under identical conditions. After the complete dehydrogenation

DOI: 10.1021/acscatal.5b01121
ACS Catal. 2015, 5, 6099−6110

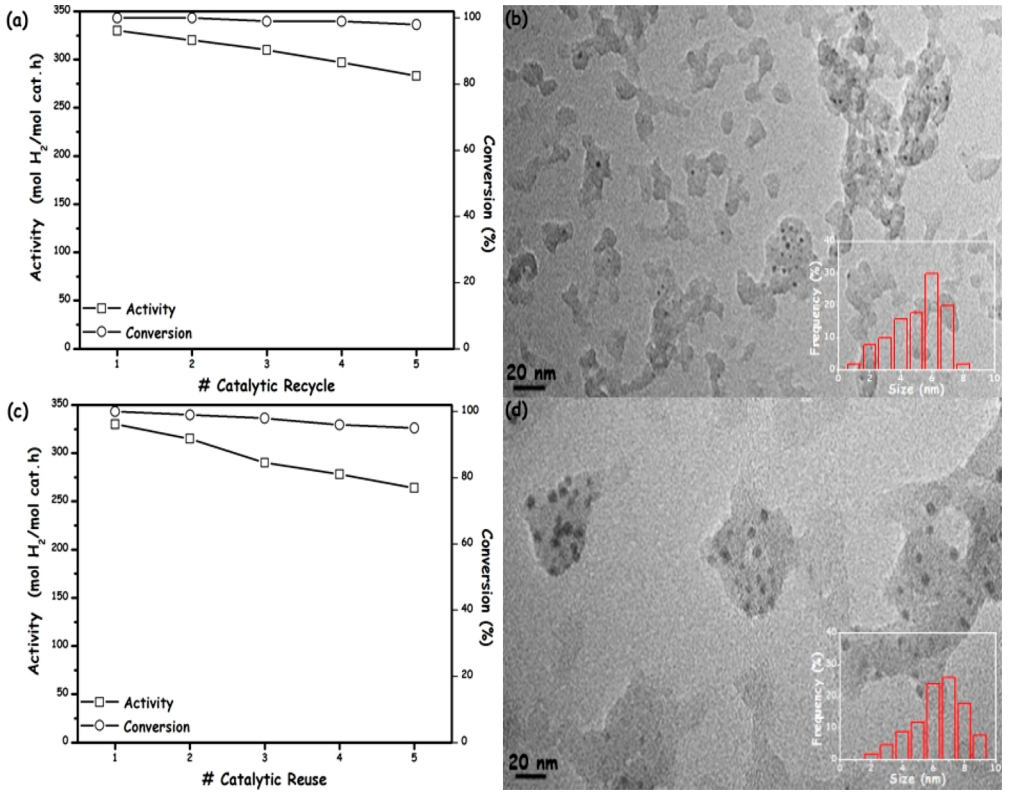

Figure 5. (a) Activity and conversion versus number of catalytic recycles for $Pd_{0.44}Ag_{0.19}$-$Mn_{0.37}$/N-SiO_2-catalyzed FA dehydrogenation in the absence of additives at 298 K, (b) TEM image of $Pd_{0.44}Ag_{0.19}$-$Mn_{0.37}$/N-SiO_2 recovered after the fifth catalytic recycle (inset shows the particle size distribution of PdAg-MnOx NPs), (c) activity and conversion versus number of catalytic reuse at 298 K, (d) TEM image of $Pd_{0.44}Ag_{0.19}$-$Mn_{0.37}$/N-SiO_2 catalyst recovered after the fifth catalytic reuse with PdAg-MnO_x NPs size distribution (inset).

of FA, PdAg-MnO_x/N-SiO_2 catalyst was isolated as a dark gray powder and bottled under nitrogen atmosphere. Then, the isolated PdAg-MnO_x/N-SiO_2 catalyst was redispersed in the aqueous FA solution. This redispersed catalyst preserved 80% of its initial activity with a 95% conversion of FA to CO_2 and H_2 even after the fifth catalytic reuse (Figure 5c).

TEM analysis of PdAg-MnO_x/N-SiO_2 samples recovered after the fifth consecutive catalytic run of the recycling and reusability experiments (Figure 5b and Figure 5d) show a slight increase in the average particle size of PdAg-MnO_x NPs (6.8 and 7.9 nm, respectively), consistent with the minor decrease in the activity at the end of these experiments. Moreover, ICP-OES and elemental analysis of used and isolated PdAg-MnO_x/N-SiO_2 catalyst samples and reaction solutions indicated that (*i*) metal and $-NH_2$ contents of the catalysts remained intact after use and (*ii*) leaching of metals and/or surface grafted amines into the reaction solution was not observed. Additionally, removing the PdAg-MnO_x/N-SiO_2 catalyst from the reaction solution can completely stop the dehydrogenation of FA. These results are indicative of the high stability of PdAg-MnO_x NPs against agglomeration and leaching throughout the catalytic runs.

Effect of Surface Grafted Amine Groups on the Catalytic Activity. In a series of additional experiments, we also compared the catalytic activities of PdAg-MnO_x/N-SiO_2, which were functionalized with different amounts of amine groups, in the additive-free dehydrogenation of FA under identical reaction conditions in order to understand the effect of the surface-grafted amine functionalities on the catalytic reactivity (Figure S11). We found that amine-free SiO_2-supported PdAg-MnO_x catalyst ($Pd_{0.41}Ag_{0.20}$-$Mn_{0.39}$/SiO_2) provides the lowest gas generation rate (6.35 mL/min) and the catalytically optimum amine loading is 0.98 mmol NH_2/g, where the maximum gas generation rate can be achieved by $Pd_{0.44}Ag_{0.19}$-$Mn_{0.37}$ NPs (30.8 mL/min).

The limited reactivity of $Pd_{0.41}Ag_{0.20}$-$Mn_{0.39}$ NPs supported on amine-free SiO_2 can be explained by the absence of $-NH_2$ functionalities on the support material, which may have a direct impact on the FA adsorption/storage process as well as the nucleation and growth of the PdAg and MnO_x NPs on the support surface (Figure S12). In a recent study, Yamashita et al.[45] reported that a resin bearing $-N(CH_3)_2$ acted as a significantly more efficient organic support material in the catalytic decomposition of FA than those bearing $-SO_3H$, $-COOH$, and $-OH$ for Pd or Ag@Pd NPs. Their mechanistic studies revealed that O−H bond cleavage in FA is facilitated by the $-N(CH_3)_2$ functionalities leading to the formation of metal-bound formate species along with a $-[N(CH_3)_2H]^+$ species, followed by the dehydrogenation of the metal-bound formate, producing H_2 and CO_2. In the light of these results, it is reasonable to propose that the existence of surface-grafted amine functionalities in the currently exploited support material efficiently acts as a proton scavenger providing a basic environment around the PdAg-MnO_x NPs. It is feasible that amine-grafted SiO_2 surface may provide an adsorption reservoir where the generated formate species on the support surface can spillover on the active PdAg-MnO_x domains. Dissociative adsorption of FA and the $-NH_2$-facilitated O−H bond scission is followed by the consecutive C−H bond cleavage from the metal-bound formate intermediate.

On the other hand, the lower activity of the catalysts in Figure S11 (see Supporting Information) with high amine

DOI: 10.1021/acscatal.5b01121
ACS Catal. 2015, 5, 6099−6110

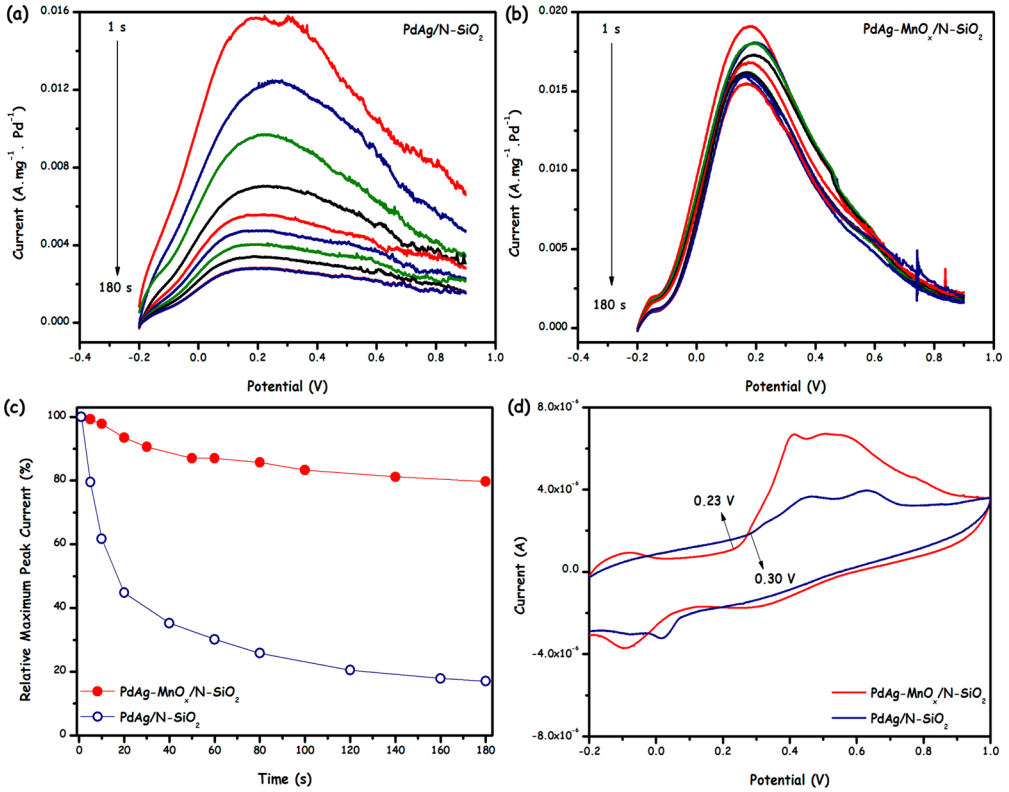

Figure 6. LSV measurements on (a) PdAg/N-SiO_2 and (b) PdAg-MnO_x/N-SiO_2 catalysts in 0.5 M H_2SO_4 + 1 M HCOOH solution with a 10 mV s^{-1} scan rate, (c) the relative maximum peak current vs time graph for PdAg/N-SiO_2 and PdAg-MnO_x/N-SiO_2 catalysts, (d) CO-stripping voltammograms for PdAg/N-SiO_2 and PdAg-MnO_x/N-SiO_2 catalysts in H_2SO_4 solution with a 10 mVs^{-1} scan rate.

loadings (i.e., > 1 mmol NH_2/g) can be attributed to two main factors, namely, the decreasing particle size of PdAg-MnO_x NPs on the support surfaces and the poisoning of the PdAg-MnO_x NPs by the excessive amount of surface $-NH_2$ functionalities covering these NPs. As shown by the TEM images given in Figure S12, PdAg-MnO_x NP size distribution can be fine-tuned by changing the coverage of the surface-grafted amine groups. Figure S12 clearly indicates that the particle size of PdAg-MnO_x NPs decreases with the increase in amine concentration. Decreasing particle size may increase the surface concentration of point defects (e.g., corner atoms, kinks, etc.) as well as extended defects (e.g., steps) on the PdAg-MnO_x NPs, which may in turn create coordinatively unsaturated sites with a high affinity toward catalytic poisons such as CO. Similarly, such defect sites may also adsorb other reactants and/or products in an adversely strong manner disfavoring the Sabatier principle.[46]

The influence of the type of the support material was also investigated by synthetically replacing N-SiO_2 with some of the ubiquitous support materials used in catalysis such as Al_2O_3, TiO_2 and C. The catalytic activities of $Pd_{0.37}Ag_{0.17}$-$Mn_{0.46}$/Al_2O_3, $Pd_{0.38}Ag_{0.20}$-$Mn_{0.32}$/TiO_2, $Pd_{0.40}Ag_{0.20}$-$Mn_{0.40}$/C, and $Pd_{0.44}Ag_{0.19}$-$Mn_{0.37}$/N-SiO_2 catalysts prepared by the same method were investigated in the additive-free FA dehydrogenation under identical conditions (Figure S13). The activity was observed to decrease in the following order: $Pd_{0.44}Ag_{0.19}$-$Mn_{0.37}$/N-SiO_2 (30.8 mL/min) > $Pd_{0.40}Ag_{0.20}$-$Mn_{0.40}$/C (10.7 mL/min) > $Pd_{0.37}Ag_{0.17}$-$Mn_{0.46}$/Al_2O_3 (4.32 mL/min) > $Pd_{0.38}Ag_{0.20}$-$Mn_{0.32}$/TiO_2 (2.1 mL/min). The formation of large-sized PdAg-MnO_x NPs (i.e., sintering) and the lack of $-NH_2$ functionalities could be responsible for the significantly lower performances of such catalysts (Figure S14).

Influence of MnO_x Nanoparticles on Poisoning Resistivity of PdAg Alloy Nanoparticles. The enhancement of Pd activity in FA dehydrogenation through Ag incorporation has already been reported for Ag@Pd[18] and PdAg[23] NPs, in which the activity increase has been attributed to a synergic effect.[47] In order to shed some light on the effect of MnO_x NPs, we conducted linear sweep voltammetry (LSV), CO stripping voltammetry, and in situ FTIR analyses.

(i). Linear Sweep Voltammetry (LSV) Analyses. We first performed LSV measurements on PdAg/N-SiO_2 and PdAg-MnO_x/N-SiO_2 catalysts to explore their stability in the electro-oxidation of formic acid. As described in detail in the Experimental Section, the catalysts were electrochemically pretreated before the LSV measurements by using a bias potential of 0.0 V for 0−180 s, where CO and OH intermediates form and bind to the active surface sites of catalysts.[48−50] Afterward, LSV measurements were conducted on the poisoned catalysts surfaces, in which the maximum current versus potential values were recorded as a function of the poisoning time (Figure 6a and Figure 6b). It is clearly seen that PdAg-MnO_x/N-SiO_2 catalyst has characteristically higher activity than PdAg/N-SiO_2 toward formic acid oxidation in terms of peak current values. Additionally, investigation of the relative peak current versus poisoning time (Figure 6c) suggests that although PdAg/N-SiO_2 almost completely loses its initial activity upon 180 s of poisoning; PdAg-MnO_x/N-SiO_2 catalyst retains >85% of its initial activity after an identical poisoning treatment.

The recent comprehensive ^{13}C NMR and ATR-IR studies[51] using formate as a surface probe for metal nanoparticles have shown that (*i*) adsorption of formic acid on metal nanoparticles

DOI: 10.1021/acscatal.5b01121
ACS Catal. 2015, 5, 6099−6110

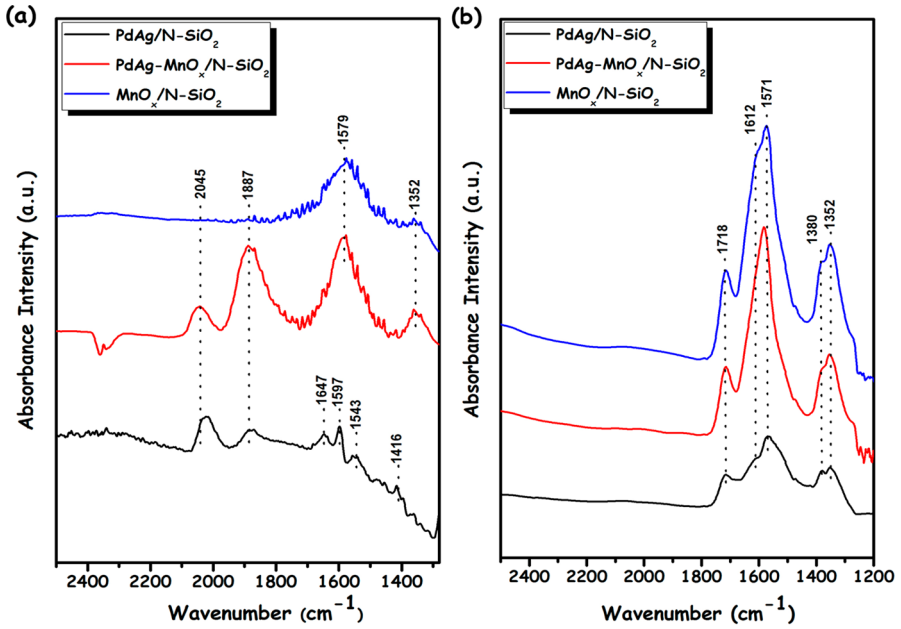

Figure 7. (a) In situ FTIR spectra acquired upon CO adsorption (20.0 Torr of CO exposure for 10 min at 323 K) on $PdAg/N\text{-}SiO_2$, $PdAg\text{-}MnO_x/N\text{-}SiO_2$ and $MnO_x/N\text{-}SiO_2$. (b) In situ FTIR spectra acquired upon formic acid adsorption (5.0 Torr of FA exposure for 5 min at 323 K) on CO prepoisoned $PdAg/N\text{-}SiO_2$, $PdAg\text{-}MnO_x/N\text{-}SiO_2$ and $MnO_x/N\text{-}SiO_2$. All of the spectra were acquired at 323 K in vacuum (10^{-3} Torr).

during FA decomposition gives three modes of adsorbed formates; (bridging, linear, and multilinear), and (*ii*) formate with OCO group, binds to surface metal atoms in a manner very similar to carbon monoxide. For this reason, as in the case of previously reported works,[52] in which FA was selectively dehydrogenated to CO_2 + H_2 and no CO was generated, we performed CO stripping voltammetry and in situ FTIR analyses by using CO as a probe molecule to understand the influence of MnO_x on the poisoning resistivity of PdAg alloy nanoparticles.

(ii). CO-Stripping Voltammetry Analyses. Figure 6d gives CO-stripping voltammograms for $PdAg/N\text{-}SiO_2$ and $PdAg\text{-}MnO_x/N\text{-}SiO_2$ catalysts (for clarity, only first scans were compared, see Figure S15 and S16 for complete voltammograms). The onset potentials were found to be 0.30 and 0.23 V for $PdAg/N\text{-}SiO_2$ and $PdAg\text{-}MnO_x/N\text{-}SiO_2$ (ΔV_{COads} = 70 mV), respectively. By considering various previous studies,[52−57] where even smaller energy differences ($\Delta V_{COads} \leq$ 70 mV) were reported, this result clearly demonstrates that the CO poisoning resistance of PdAg alloy NPs can be significantly enhanced by the promotional effect of MnO_x NPs. Another significant feature of the CO-stripping voltammograms given in Figure 6d is the fact that MnO_x-promoted catalyst releases a significantly greater amount of CO during the voltage sweep.

As shown in the Table S1 (see Supporting Information), specific surface area is not the primary factor in CO storage, as MnO_x incorporation does not significantly alter it. This observation is in perfect agreement with the current in situ FTIR experiments that will be discussed in the forthcoming section suggesting that MnO_x domains function as sacrificial sites, which can efficiently store CO in the form of carbonates, preventing the catalytic poisoning of the PdAg active sites. It is worth mentioning that in the presence of MnO_x, although a significantly greater quantity of catalytic poisoning species (i.e., CO) is captured by the catalyst surface, these antagonistic species can be very readily and reversibly removed from the catalyst surface, evident by the lower CO-oxidation onset potential for $PdAg\text{-}MnO_x/N\text{-}SiO_2$ catalysts with respect to that of $PdAg/N\text{-}SiO_2$ (Figure 6d).

(iii). In Situ FTIR Spectroscopy. In situ FTIR experiments were performed (Figure 7) to investigate the relative CO poisoning characteristics of different adsorption sites on the $PdAg\text{-}MnO_x/N\text{-}SiO_2$ catalyst at the molecular level. It is well-known that Ag and Pd can dissolve in each other to form bimetallic alloys with a wide range of compositions.[58] Former comprehensive FTIR spectroscopic studies on supported PdAg bimetallic NPs and PdAg ultrathin films demonstrated that CO interacts very weakly with the Ag adsorption sites (irrespective of the Ag content of the bimetallic NP) leading to vibrational features with intensities that are typically below the experimental detection limit;[59−63] while the interaction of CO with the Pd adsorption sites is significantly strong. CO vibrational signatures on monometallic Ag NPs deposited on oxide surfaces typically appear at ≥2169 cm^{-1}.[64] Before starting the in situ FTIR analyses, the catalytic reactivity of $PdAg\text{-}MnO_x/N\text{-}SiO_2$ catalyst annealed under vacuum (<1x 10^{-3} Torr) at 400 K for 2 h was checked in the catalytic dehydrogenation of FA in order to show this pretreatment does not significantly affect the catalytic nature of $PdAg\text{-}MnO_x/N\text{-}SiO_2$ catalyst. The result of this control experiment revealed that the catalytic activity of $PdAg\text{-}MnO_x/N\text{-}SiO_2$ catalyst is not affected by this pretreatment as annealed $PdAg\text{-}MnO_x/N\text{-}SiO_2$ catalyst gave almost the same activity and conversion values with that of fresh $PdAg\text{-}MnO_x/N\text{-}SiO_2$ catalyst (Figure S17).

CO adsorption on PdAg reveals unique vibrational features dissimilar to monometallic Pd surfaces. Pd and PdAg nanoparticles exhibit a truncated-cuboctahedral geometry (*Wulff Polyhedron*) exposing (111) facets with a minor contribution from (100) facets.[65−67] CO/Pd(111) yields ν_{CO} at ca. 2110, 1960 and 1895−1810 cm^{-1} corresponding to atop (linear), bridging, and 3-fold adsorption geometries, respectively.[66−68] CO/Pd(100) leads to exclusively bridging adsorption (1997−1807 cm^{-1}).[66,67] Figure 7a presents in situ FTIR spectra recorded after the saturation of $PdAg/N\text{-}SiO_2$, PdAg-

DOI: 10.1021/acscatal.5b01121
ACS Catal. 2015, 5, 6099−6110

MnO_x/SiO_2, and MnO_x/SiO_2 surfaces with CO at 323 K. Ag incorporation into the Pd structure strongly alters the CO adsorption on the atop and bridging Pd sites evident by ν_{CO} at 2045 and 1887 cm^{-1} (Figure 7a) with a characteristic red shift ($\Delta\nu_{CO}$ = 65−73 cm^{-1}) compared to that of Pd(111) (i.e., 2110 and 1960 and cm^{-1}, respectively[66]). This is in perfect agreement with a former study,[69] demonstrating the correlation between the red-shift in ν_{CO} upon Ag incorporation into the Pd lattice and weakening of the CO adsorption strength. Similarity in the magnitude of the red shift for atop and bridging Pd adsorption sites suggests that Ag is rather uniformly distributed in the bimetallic NP, influencing atop and bridging Pd adsorption sites alike.

Weakening of the CO adsorption strength is very critical for FA dehydrogenation, as it directly indicates the increased tolerance against CO poisoning. Strongly adsorbed CO on the defective monometallic Pd particles may lead to "*adsorbate-induced surface reconstruction*" resulting in the disintegration (i.e., leaching) of the monometallic Pd particles.[59] Decreasing the CO adsorption strength via alloying with Ag increases the stability and catalytic lifetime as demonstrated by the stability and reusability tests (vide infra). Lack of ν_{CO} at ≥2169 cm^{-1} in Figure 7a suggests that Ag sites are either not exposed or CO adsorption on Ag is weak. Furthermore, 1887 cm^{-1} signal of PdAg-MnO_x/N-SiO_2 is much stronger than that of the PdAg/N-SiO_2. In order to explain this observation, one can argue that PdAg NPs located on the MnO_x promoted catalyst might have a larger average particle size, thus exposing larger (111) and (100) facets favoring bridging sites. However, PdAg-MnO_x/N-SiO_2 does not have a larger average particle size than PdAg/N-SiO_2 (Supporting Information Figure S5). As an alternative explanation, variation of the surface composition and surface morphology of the PdAg alloy NPs upon MnO_x promotion can be considered. In the presence of MnO_x, number of exposed Ag sites on the surface of the bimetallic NPs may decrease, along with the number of coordinatively unsaturated sites (i.e., defects), leading to more ordered (111)/(100) domains and larger (100) facets on the catalyst surface favoring high-coordination CO adsorption without increasing the average particle size. It is feasible that CO adsorption on this Ag-doped and ordered (111)/(100) terraces in proximity of MnO_x could be energetically less favorable than that of the MnO_x-free catalyst. This is in very good agreement with the CO-SV measurements given in Figure 6d, suggesting that CO is removed much readily in the presence of MnO_x. Thus, it is plausible that MnO_x domains may modify the surface composition and electronic structure of the PdAg NP alloy with respect to its MnO_x-free counterpart.

FTIR spectra for CO adsorption on PdAg-MnO_x/N-SiO_2 and MnO_x/N-SiO_2 (Figure 7a) show two broad and intense features at 1579 and 1352 cm^{-1} associated with carbonate species formed upon adsorption of CO on the Lewis basic sites of MnO_x and SiO_2. Weakness of the carbonate signals in the absence of MnO_x implies that carbonates are formed almost exclusively on the MnO_x domains, which act as *"pinning/anchoring sites"* for CO and function as sacrificial sites against CO poisoning of the precious metal sites. Relatively more intense carbonate features on PdAg-MnO_x/N-SiO_2 compared to MnO_x/N-SiO_2 can be explained by the CO spillover from the PdAg NP to the MnO_x domains. For PdAg/N-SiO_2, the shoulder at 1850−1700 can be assigned to carbonyls on bridging and 3-fold sites of PdAg, whereas features at ≤1650 cm^{-1} can be attributed to carbonates on N-SiO_2. Competitive adsorption of FA and CO was also monitored via in situ FTIR (Figure 7b) revealing features at ca. 1718, 1612, 1571, 1380, and 1352 cm^{-1} assigned to molecular FA[70−72] and bidentate/monodentate formates ($HCOO^-$).[70−73] PdAg/N-SiO_2 shows relatively weak FA/formate features suggesting that strongly bound CO on PdAg prevents FA adsorption/formate generation. Carbonates formed on N-SiO_2 also hinder the adsorption of FA on the support. Thus, in the absence of MnO_x, CO poisoning severely hinders the FA uptake capacity. Note that this behavior cannot be explained by differences in surface areas, as the catalysts in Figure 7 have comparable BET surface area values (Supporting Information Table S1). PdAg-MnO_x/N-SiO_2 can absorb a significantly greater quantity of FA/formate even after extended CO exposure (Figure 7b). Incorporation of MnO_x can provide supplementary FA/formate adsorption sites, boosting the FA/formate uptake capacity. This is justified by the control experiments performed on MnO_x/N-SiO_2 lacking any PdAg (Figure 7b). CO capture by MnO_x enables the PdAg to remain available for FA adsorption/dissociation where the generated formates can reversibly spillover on/from the MnO_x and N-SiO_2 domains.

CONCLUSIONS

In summary, PdAg-MnO_x/N-SiO_2 catalyst prepared in this study reveals a remarkable catalytic performance in terms of activity (330 mol H_2·mol catalyst^{-1}·h^{-1}) and excellent conversion (>99%) in the additive-free dehydrogenation of FA. Moreover, PdAg-MnO_x/N-SiO_2 shows excellent stability against agglomeration, leaching, and CO poisoning, rendering it highly recyclable and reusable. Incorporation of Ag sites into Pd NPs yields PdAg alloys, decreasing the CO adsorption strength, increasing CO poisoning tolerance, suppressing the adsorbate (i.e., CO) induced reconstruction and disintegration/leaching of Pd NPs. MnO_x provides sacrificial CO anchoring sites forming carbonates. As a result, PdAg sites remain available for the dehydrogenation of FA for an extended duration. This uniquely active, selective, and reusable catalyst has a strong potential to be exploited in practical/technological applications, where FA is utilized as a viable hydrogen carrier in mobile fuel cell applications.

ASSOCIATED CONTENT

Supporting Information

The Supporting Information is available free of charge on the ACS Publications website at DOI: 10.1021/acscatal.5b01121.

Figures S1−S17 include information for the catalytic activity tests, control experiments, CTEM images, CV results, and calculation methods (PDF)

AUTHOR INFORMATION

Corresponding Author

*(M.Z.) E-mail: zmehmet@yyu.edu.tr. Fax: 90 432 225 18 06. Website: www.nanomatcat.com.

Notes

The authors declare no competing financial interest.

ACKNOWLEDGMENTS

M.Z. thanks the Research Fund of Yüzüncü Yıl University for the financial support to his research laboratory. Additionally, the partial supports by Fevzi Akkaya Scientific Activities Support Fund (FABED), Science Academy, and Turkish Academy of Sciences (TUBA) are gratefully acknowledged.

DOI: 10.1021/acscatal.5b01121
ACS Catal. 2015, 5, 6099−6110

REFERENCES

(1) Muradov, N.; Vezirolu, T. *Int. J. Hydrogen Energy* **2005**, *30*, 225−237.
(2) Schlapbach, L.; Züttel, A. *Nature* **2001**, *414*, 353−358.
(3) Turner, J. A. *Science* **1999**, *285*, 687−689.
(4) Enthaler, S.; von Langermann, J.; Schmidt, T. *Energy Environ. Sci.* **2010**, *3*, 1207−1217.
(5) Yadav, M.; Xu, Q. *Energy Environ. Sci.* **2012**, *5*, 9698−9725.
(6) Kordesch, K. V.; Simader, G. R. *Chem. Rev.* **1995**, *95*, 191−207.
(7) Myers, T. W.; Berben, L. A. *Chem. Sci.* **2014**, *5*, 2771−2777.
(8) Zell, T.; Butschke, B.; Ben-David, Y.; Milstein, D. *Chem. - Eur. J.* **2013**, *19*, 8068−8072.
(9) Wang, W.-H.; Xu, S.; Manaka, Y.; Suna, Y.; Kambayashi, H.; Muckerman, J. T.; Fujita, E.; Himeda, Y. *ChemSusChem* **2014**, *7*, 1976−1983.
(10) Johnson, T. C.; Morris, D. J.; Wills, M. *Chem. Soc. Rev.* **2010**, *39*, 81−88.
(11) Grasemann, M.; Laurenzcy, G. *Energy Environ. Sci.* **2012**, *5*, 8171−8181.
(12) Fukuzumi, S.; Kobayashi, T.; Suenobu, T. *J. Am. Chem. Soc.* **2010**, *132*, 1496−1497.
(13) Boddien, A.; Mellmann, D.; Gartner, F.; Jackstell, R.; Junge, H.; Dyson, P. J.; Laurenczy, G.; Ludwig, R.; Beller, M. *Science* **2011**, *333*, 1733−1736.
(14) Scholten, J. D.; Prechtl, M. H. G.; Dupont, J. *ChemCatChem* **2010**, *2*, 1265−1270.
(15) Zhu, Q. L.; Tsumori, N.; Xu, Q. *Chem. Sci.* **2014**, *5*, 195−199.
(16) Zhou, X.; Huang, Y.; Xing, W.; Liu, C.; Liao, J.; Lu, T. *Chem. Commun.* **2008**, 3540−3542.
(17) Bi, Q. Y.; Du, X. L.; Liu, Y. M.; Cao, Y.; He, H. Y.; Fan, K. N. *J. Am. Chem. Soc.* **2012**, *134*, 8926−8933.
(18) Tedsree, K.; Li, T.; Jones, S.; Chan, C. W. A.; Yu, K. M. K.; Bagot, P. A. J.; Marquis, E. A.; Smith, G. D. W.; Tsang, S. C. E. *Nat. Nanotechnol.* **2011**, *6*, 302−307.
(19) Wang, Z. L.; Yan, J. M.; Wang, H. L.; Ping, Y.; Jiang, Q. *J. Mater. Chem. A* **2013**, *1*, 12721−12725.
(20) Wang, Z. L.; Yan, J. M.; Ping, Y.; Wang, H. L.; Zheng, W. T.; Jiang, Q. *Angew. Chem., Int. Ed.* **2013**, *52*, 4406−4409.
(21) Wang, Z.- L.; Wang, H.-L.; Yan, J. M.; Ping, Y.; O, S.-I.; Li, S.-j.; Jiang, Q. *Chem. Commun.* **2014**, *50*, 2732−2734.
(22) Metin, Ö.; Sun, X.; Sun, S. *Nanoscale* **2013**, *5*, 910−912.
(23) Zhang, H.; Metin, Ö.; Su, D.; Sun, S. *Angew. Chem., Int. Ed.* **2013**, *52*, 3681−3684.
(24) Bulut, A.; Yurderi, M.; Karatas, Y.; Zahmakiran, M.; Kivrak, H.; Gulcan, M.; Kaya, M. *Appl. Catal., B* **2015**, *164*, 324−333.
(25) Yan, J.-M.; Wang, Z.-L.; Gu, L.; Li, S.-J.; Wang, H.-L.; Zheng, W.-T.; Jiang, Q. *Adv. Energy Mater.* **2015**, *5*, 1500107.
(26) Yurderi, M.; Bulut, A.; Caner, N.; Celebi, M.; Kaya, M.; Zahmakiran, M. *Chem. Commun.* **2015**, *51*, 11417−11420.
(27) Gu, X.; Lu, Z.-H.; Jiang, H.-L.; Akita, T.; Xu, Q. *J. Am. Chem. Soc.* **2011**, *133*, 11822−11825.
(28) Loges, B.; Boddien, A.; Junge, H.; Beller, M. *Angew. Chem., Int. Ed.* **2008**, *47*, 3962−3965.
(29) Bielinski, E. A.; Lagaditis, P. O.; Zhang, Y.; Mercado, B. Q.; Würtele, C.; Bernskoetter, W. H.; Hazari, N.; Schneider, S. *J. Am. Chem. Soc.* **2014**, *136*, 10234−10237.
(30) Taylor, I.; Howard, A. G. *Anal. Chim. Acta* **1993**, *271*, 77−84.
(31) White, R. J.; Luque, R.; Budarin, V. L.; Clark, J. H.; Macquarrie, D. J. *Chem. Soc. Rev.* **2009**, *38*, 481−494.
(32) Chen, W.; Kim, J.; Xu, L.-P.; Sun, S.; Chen, S. *J. Phys. Chem. C* **2007**, *111*, 13452−13459.
(33) Jiang, K.; Cai, W. B. *Appl. Catal., B* **2014**, *147*, 185−192.
(34) Say, Z.; Vovk, E. I.; Bukhtiyarov, V. I.; Ozensoy, E. *Appl. Catal., B* **2013**, *142-143*, 89−100.
(35) Zhang, Y.; He, X.; Ouyang, J.; Yang, H. *Sci. Rep.* **2013**, *3*, 1−5.
(36) Prieto, P.; Nistor, V.; Nouneh, K.; Oyama, M.; Abd-Lefdil, M.; Diaz, R. *Appl. Surf. Sci.* **2012**, *258*, 8807−8813.
(37) Kang, M.; Park, E. D.; Kim, J. M.; Yie, J. E. *Appl. Catal., A* **2007**, *327*, 261−269.
(38) Xingyi, W.; Qian, K.; Dao, L. *Appl. Catal., B* **2009**, *86*, 166−175.
(39) Bondi, J. F.; Oyler, K. D.; Ke, X.; Schiffer, P.; Schaak, R. E. *J. Am. Chem. Soc.* **2009**, *131*, 9144−9145.
(40) Si, P. Z.; Bruck, E.; Zhang, Z. D.; Tegus, O.; Zhang, W. S.; Buschow, K. H. J.; Klaasse, J. C. P. *Mater. Res. Bull.* **2005**, *40*, 29−37.
(41) Hutchison, J. E.; Woehrie, G. H.; Özkar, S.; Finke, R. G. *Turkish J. Chem.* **2006**, *30*, 1−13.
(42) Li, Y.; Afzaal, M.; O'Brien, P. *J. Mater. Chem.* **2006**, *16*, 2175−2181.
(43) Liu, L.; Liang, H.; Yang, H.; Wei, J.; Yang, Y. *Nanotechnology* **2011**, *22*, 015603.
(44) Connors, K. A. *Theory of Chemical Kinetics*; VCH Publishers: New York, 1990.
(45) Mori, K.; Dojo, M.; Yamashita, H. *ACS Catal.* **2013**, *3*, 1114−1119.
(46) Sabatier, P. *Ber. Dtsch. Chem. Ges.* **1911**, *44*, 1984−1988.
(47) Yoo, J. S.; Abild-Pedersen, F.; Norskov, J. K.; Studt, F. *ACS Catal.* **2014**, *4*, 1226−1233.
(48) Cai, J.; Huang, H.; Huang, B.; Zheng, S.; Guo, Y. *Int. J. Hydrogen Energy* **2014**, *39*, 798−807.
(49) Zhang, S.; Shao, Y.; Yin, G.; Lin, Y. *Angew. Chem., Int. Ed.* **2010**, *49*, 2211−2213.
(50) Martinez-Huerta, M. V.; Rodriguez, L.; Tsiouvaras, N.; Pena, M. A.; Fierro, J. L. G.; Pastor, E. *Chem. Mater.* **2008**, *20*, 4249−4259.
(51) Tedsree, K.; Kong, A. T. S.; Tsang, S. C. *Angew. Chem., Int. Ed.* **2009**, *48*, 1443−1446.
(52) Qin, Y.-L.; Wang, J.; Meng, F.-Z.; Wang, L.-M.; Zhang, X.-B. *Chem. Commun.* **2013**, *49*, 10028−10030. Waszczuk, P.; Barnard, T. M.; Rice, C.; Masel, R. I.; Wieckowski, A. *Electrochem. Commun.* **2002**, *4*, 599−603.
(53) Zhou, W.; Lee, J. Y. *Electrochem. Commun.* **2007**, *9*, 1725−1729.
(54) Lee, H.; Habas, S. E.; Somorjai, G. A.; Yang, P. *J. Am. Chem. Soc.* **2008**, *130*, 5406−5407.
(55) Waszczuk, P.; Barnard, T. M.; Rice, C.; Masel, R. I.; Wieckowski, A. *Electrochem. Commun.* **2002**, *4*, 599−603.
(56) Rao, C. V.; Cabrera, C. R.; Ishikawa, Y. *J. Phys. Chem. C* **2011**, *115*, 21963−21970.
(57) Zhang, G.; Wang, Y.; Wang, X.; Chen, Y.; Zhou, Y.; Tang, Y.; Lu, L.; Bao, J.; Lu, T. *Appl. Catal., B* **2011**, *102*, 614−619.
(58) Chen, J. G.; Menning, C. A.; Zellner, M. B. *Surf. Sci. Rep.* **2008**, *63*, 201−209.
(59) Terekhina, O.; Roduner, E. *J. Phys. Chem. C* **2012**, *116*, 6973−6979.
(60) Heinrichs, B.; Noville, F.; Schoebrechts, J. P.; Pirard, J. P. *J. Catal.* **2000**, *192*, 108−118.
(61) Soma-Noto, Y.; Sachtler, W. M. H. *J. Catal.* **1974**, *32*, 315−324.
(62) Huang, W.; Lobo, R. F.; Chen, J. G. *J. Mol. Catal. A: Chem.* **2008**, *283*, 158−165.
(63) Ma, Y.; Diemant, T.; Bansmann, J.; Behm, R. J. *Phys. Chem. Chem. Phys.* **2011**, *13*, 10741−10747.
(64) Bechoux, K.; Marie, O.; Daturi, M.; Delahay, G.; Petitto, C.; Rousseau, S.; Blanchard, G. *Catal. Today* **2012**, *197*, 155−160.
(65) Henry, C. R. *Surf. Sci. Rep.* **1998**, *31*, 235−240.
(66) Ozensoy, E.; Goodman, D. W. *Phys. Chem. Chem. Phys.* **2004**, *6*, 3765−3771.
(67) Ozensoy, E.; Min, B. K.; Santra, A. K.; Goodman, D. W. *J. Phys. Chem. B* **2004**, *108*, 4351−4357.
(68) Ozensoy, E.; Vovk, E. I. *Top. Catal.* **2013**, *56*, 1569−1575.
(69) Ma, Y.; Diemant, T.; Bansmann, J.; Behm, R. J. *Phys. Chem. Chem. Phys.* **2011**, *13*, 10741−10746.
(70) Millar, G. J.; Rochester, C. H.; Waugh, K. C. *J. Chem. Soc., Faraday Trans.* **1991**, *87*, 1491−1495.
(71) Monti, D. M.; Cant, N. W.; Trimm, D. L.; Wainright, M. S. *J. Catal.* **1986**, *100*, 17−27.
(72) Burch, R.; Chalker, S.; Pritchard, J. *J. Chem. Soc., Faraday Trans.* **1991**, *87*, 193−203.
(73) Popova, G. Y.; Chesalov, Y. A.; Sadovskaya, E. M.; Andrushkevich, T. V. *J. Mol. Catal. A: Chem.* **2012**, *357*, 148−159.

DOI: 10.1021/acscatal.5b01121
ACS Catal. 2015, 5, 6099−6110